Large-Eddy Simulation of Kerosene Spray Ignition in a Simplified Aeronautic Combustor

L Hervo, J M Senoner, A Biancherin, B Cuenot

Noname manuscript No.
(will be inserted by the editor)

Large-Eddy Simulation of Kerosene Spray Ignition in a Simplified Aeronautic Combustor

L. Hervo · J.M. Senoner · A. Biancherin · B. Cuenot

the date of receipt and acceptance should be inserted later

Abstract The current work presents the Large Eddy Simulation (LES) of a kerosene spray ignition phase in a simplified aeronautical combustor for which detailed experimental data are available. The carrier phase is simulated using an unstructured multi-species compressible Navier-Stokes solver while the dispersed liquid phase is modeled with a Lagrangian approach. An energy deposition model neglecting the presence of a plasma phase in the very first instants of the energy deposition process, a reduced kinetic scheme and a simplified spray injection model are combined to achieve both a reasonable computational expense and a satisfactory overall accuracy. Following a brief description of the validation of these models, non reactive gaseous and two-phase flow LES's of the target combustor are performed. Excellent agreement with experiments is observed for the non reactive gaseous simulations. The dispersed phase velocity fields are also well reproduced while discrepancies appear for the spatial size distribution of the particles. Finally, numerical snapshots of a successful ignition phase are shown and discussed.

1 Introduction

In order to reduce the consumption and the pollutant emissions of their engines, aircraft manufacturers are testing new combustor designs that may be operated safely in a lean regime. However, lean premixed combustors may be difficult to ignite, especially at high altitude conditions. Today, numerous experimental tests are required to ensure ignition capability in the whole operating domain. In this context, the availability of accurate numerical tools

L. Hervo · J.-M. Senoner · A. Biancherin
ONERA, The French Aerospace Lab, Toulouse, France
E-mail: jean-mathieu.senoner@onera.fr

B. Cuenot
CERFACS, Toulouse, France

could provide better physical insight into ignition phenomena, shorten the design cycles of new combustors and reduce the necessity of expensive test campaigns. However, simulating the ignition phase of an aeronautical combustor is a difficult task as this event is a complex process involving a variety of physical phenomena. Five main phases may be distinguished during an ignition sequence [22]:

- The first phase is characterized by the energy deposition process. From a technological point of view, ignition is still mostly initiated with spark plugs in modern aircraft engines, despite important research efforts on alternative techniques such as laser focusing, micro-waves, etc... Regardless of the device, the energy deposition is generally very localized. For aeronautical applications, local energy concentration levels are such that temperature levels exceed several tens of thousand Kelvins, leading to a local ionization of the atoms in the gas and the generation of a plasma phase. Energy deposition is also characterized by a very fast and significant pressure increase, typically of the order of several bars.
- As the pressure suddenly increases, a shock wave contributing to the expansion of the plasma generally forms. As a consequence of this expansion, the maximum temperature and pressure levels start to decrease.
- As temperature levels decrease to several thousands of Kelvins, a kernel of hot gases appears. Provided the kernel's chemical composition is favourable, it may ignite and form a flame kernel.
- The evolution of the flame kernel is then dictated by its propagation and its convection within the aeronautical combustion chamber. Furthermore, the flame kernel becomes wrinkled, stretched and strained as it evolves in a turbulent flow field. For several reasons, it may be quenched during this phase ("failed ignition") or continue to expand within the chamber until a stabilized combustion regime is attained ("successful ignition"). Therefore, ignition in turbulent flow configurations may only be defined via local probabilities.
- Additionally, real combustors are made of several burners and ignition is generally not triggered in all of them. Thus, flame propagation to all burners must also be ensured.

For single burner configurations, the main quantity of interest is the local ignition probability as a function of the operating conditions. In a first approximation, this quantity may be estimated from local properties such as the equivalence ratio, the mean and fluctuating velocity fields, etc... Models based on Reynols Averaged Navier Stokes (RANS) or time averaged Large Eddy Simulations (LES) as well as instantaneous LES flow fields or a combination of both may be found in the literature [14, 28]. Due to the continuous increase of computational resources, LES's of the ignition sequence of entire annular combustors are becoming feasible [4]. Similarly, ignition probabilities may be directly evaluated from LES's [12].

From the above phenomenological description, it follows that these simulations would need to explicitly account for the presence of a plasma in the

first instants following the energy deposition process. However, this requires coupling a Maxwell and a compressible Navier-Stokes solver [42] and is rarely done in practice. Instead, the influence of the plasma phase on the properties of the kernel of hot gases is often modelled. Duclos and Colin [10] proposed the Reynolds Averaged Navier-Sokes (RANS) AKTIM model, where the temporal evolutions of tension and current intensity within the discharge circuit are used to estimate the amount of energy supplied to the spark plug. The spark is then represented with Lagrangian tracers in order to account for the interaction with the surrounding gas. These tracers are initially carrying a vanishing amount of burnt gases, a given amount of fresh gases and an excess of energy. Whenever the excess of energy lies above a fixed threshold, the mass of burnt gases becomes equal to the mass of fresh gases and a flame kernel is initiated in the flow field. A very similar model relying on the use of Lagrangian tracers until the formation of the initial flame kernel named Spark Channel Ignition Monitoring Model (SparkCIMM) was proposed by Dahms *et al.* [9]. Once this flame kernel exceeds a characteristic size allowing its explicit resolution on the numerical grid, the SparkCIMM model is deactivated and tracked with a combustion model based on the G-equation. The AKTIM model was later adapted from the RANS to the Large Eddy Simulation (LES) context by Colin and Truffin [7] and coined Imposed Stretch Spark Ignition (ISSIM) LES model. It relies on the addition of an energy source term to the ECFM combustion model [33]. Curvature effects occurring at the subgrid scale rely on an analytical model as long as the kernel is underresolved on the numerical grid. A simpler level of modeling may be achieved by imposing a temporally and spatially varying source term to the energy equation, as done in the Energy Deposition (ED) model proposed by Enaux [11] and Lacaze [17]. In order to limit the influence of the subgrid scales in the first instants of the flame kernel formation, the authors combined their ED model with a high level of refinement in the area of energy deposition. Despite its simplicity, this approach was able to quantitatively predict the dynamics of a methane jet ignition [17].

When the fuel is supplied to the kernel of hot gases as a spray, droplet flame interactions need to be additionally taken into account. The characteristic fuel droplet evaporation time scale will generally be much larger than the characteristic chemical time scale of combustion, leading to a decrease in flame propagation speeds compared to the perfectly premixed case [27]. Moreover, spray evaporation acts as a significant heat sink and may thus favour flame extinction phenomena. More details on spray ignition may be found in the reviews by Aggarwal [2] and Mastorakos [23].

The present work aims at assessing the capabilities of an energy deposition model, reduced chemical kinetics and a global spray injection model to simulate the ignition phase of a simplified aeronautical combustor in the presence of a dispersed phase. To the authors' knowledge, numerical simulations of the entire ignition phase have not yet been published for this target configuration despite previous investigations [5, 14].

The current article is organized as follows. First, the simplified methodology used to model the energy deposition phase of the ignition process is described. Second, the target combustor is presented. The main characteristics of the Navier-Stokes solver used to simulate the non-reacting gaseous flow field within the target configuration are then detailed before presenting numerical results. Third, simulations of the dispersed two-phase flow within the target configuration are shown. Then, the simulation of a successful ignition phase is analysed. The main findings are summarized in the conclusion, followed by possible outlooks.

2 Ignition modeling

2.1 Energy deposition model

In order to approximately reproduce the phenomena leading to the formation of a kernel of hot gases in the vicinity of the electrodes of the spark plug, the Energy Deposition (ED) of Enaux [11] and Lacaze [17] is used. This model simply consists in adding an unsteady source term to the energy equation. This source term is assumed to follow a Gaussian curve in time and space [11].

$$\dot{Q} = \frac{\epsilon_i}{4\pi^2\sigma_S^3\sigma_t} e^{-\frac{1}{2}\left(\frac{r-r_0}{\sigma_S}\right)^2} e^{-\frac{1}{2}\left(\frac{t-t_0}{\sigma_t}\right)^2} \tag{1}$$

with:

$$\sigma_S = \frac{\Delta_S}{2\sqrt{\ln(10^4)}} \qquad \text{and} \qquad \sigma_t = \frac{\Delta_t}{2\sqrt{\ln(10^4)}} \tag{2}$$

where $\dot{Q}$ is the energy source term, ϵ_i is the total energy supplied to the gas by the spark plug, Δ_S and Δ_t are the length and duration where 99% of the energy is deposed thanks to the normalization constant $2\sqrt{\ln(10^4)}$, r is the distance from the center of the source term r_0, t is the time and t_0 is the instant where the power given by the spark is maximum. It was verified that the implemented numerical procedure allowed to exactly control the amount of energy supplied to the flow field over time (not shown).

2.2 Thermodynamics and transport properties

The energy supplied to the flow by the aforementioned source term leads to significant local temperature increase. As a consequence, the range of validity of most thermophysical and transport properties may be exceeded. In order to extend this range of validity, the thermodynamic properties (heat capacity, enthalpy and entropy) of the major components N_2 and O_2 are described by polynomial expressions provided by McBride *et al.* [25] and valid up to 20 000 K in the present work. However, it is important to note that these polynomial expressions only account for temperature dependencies related to the

molecular degrees of freedom although the aforementioned properties also depend on the chemical composition of the mixture. Accounting for composition changes due to endothermic ionization and dissociation processes would require dedicated kinetic mechanisms characterizing these phenomena and was considered out of the scope of the present work.

Fig. 1 displays the comparison between the modified heat capacity curve at constant pressure for nitrogen N_2 [25] used in the present numerical simulations and the reference curves available in the CEDRE software (more details on the CEDRE software are provided in section 4.1). Moreover, a comparison between the theoretical polynomial curves and the actual values retrieved from numerical simulations with imposed temperature variations is also shown for validation purposes.

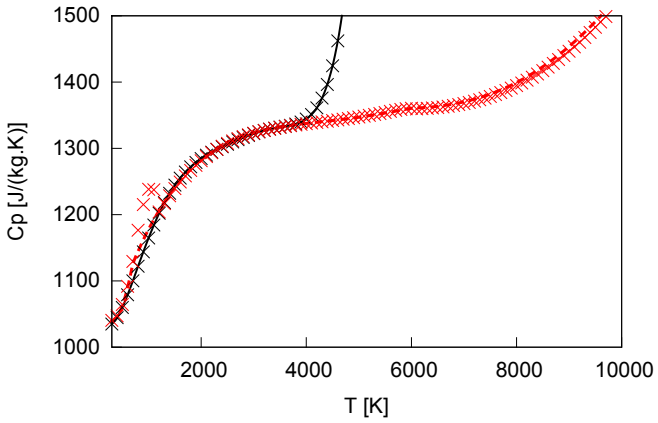

Fig. 1: Evolution of the heat capacities of N_2 over temperature according to CEDRE reference data and the data of McBride *et al.* [25]. Curves: numerical results from CEDRE simulations. Symbols: polynomial curves.

Unfortunately, the authors could not find any data to describe the thermodynamic properties of combustion products such as carbon monoxide CO, carbon dioxide CO_2 or the various fuel species at temperatures above 5000 K. The latter were therefore kept constant above this threshold value.

The transport properties of the species are described by laws commonly used and no specific modifications were applied for higher temperatures. In particular, the viscosity of the different species follows a Sutherland law while the thermal conductivity and the diffusivity of the species are calculated with the assumption of a constant Prandtl and Schmidt number. It is important to note that the approximations made for transport properties must remain consistent with those used to derive the reduced kinetic schemes to ensure a correct laminar flame speed. However, it should be possible to combine these

transport properties with different laws valid at higher temperatures and this aspect will be investigated in future work.

2.3 Validation case in laminar premixed conditions

In order to assess the capabilities of the aforementioned modeling ingredients on an elementary test case, the propagation of a laminar flame kernel in a propane-air mixture is simulated. The test case reproduces the conditions of an experiment performed by Renou and Boukhalfa [32], and was simulated by Enaux [11] with the AVBP solver. Chemical reactions are modeled with a two-step scheme reproducing correct laminar flame speeds at ambient conditions [11]. The parameters related to the energy deposition model, see eq. 1, are strictly identical to those of Enaux [11] and summarized in table 1.

Δ_S	2 mm
Δ_t	120 µs
ϵ_i	2.5 mJ

Table 1: Parameters of the energy deposition model in the numerical simulations of the laminar flame kernel propagation experiment of Renou and Boukhalfa [32]

The evolution of the flame radius over time is compared to experiment in fig. 2 where the results of Enaux [11] are also reported. The flame radius is defined as follows:

$$R = \left(\frac{12}{\pi} V_T \left(1 - \frac{Y_f^{mean}}{Y_f^0} \right) \right)^{1/3} \tag{3}$$

where V_T, Y_f^{mean} and Y_f^0 respectively denote the total volume of the computational domain, the mean and initial fuel mass fraction in this domain. As may be seen on fig. 2, the agreement between both simulations and the experiment is very good for the temporal evolution of the flame radius. An equally good agreement is observed for the flame speed, as may be seen on fig. 3. The flame propagation speed is defined as the temporal derivative of the radius according to eq. 3:

$$S_c = \frac{\rho_1}{\rho_0} \frac{dR}{dt} \tag{4}$$

with the subscripts 0 and 1 respectively denoting properties in the fresh and burnt gases.

From fig. 3, it appears that the flame propagation is extremely fast until approximately $t = 0.3$ ms after which it starts decelerating at the expected laminar flame speed of approximately $0.2\,\mathrm{m\,s^{-1}}$ at these conditions. The very fast fuel consumption in the first instants may either be due to auto-ignition in the expanding kernel of hot gases or the high stretching of the flame kernel.

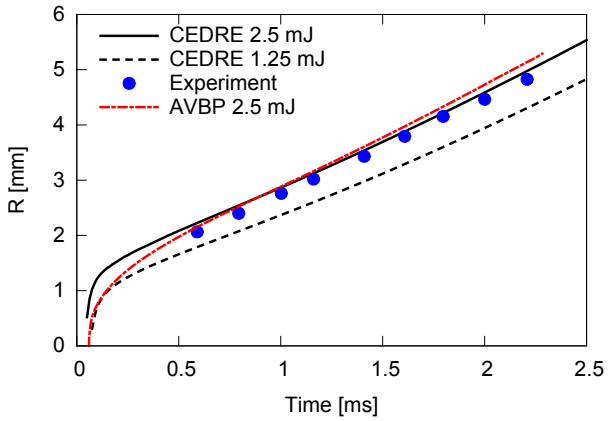

Fig. 2: Evolution of the flame kernel radius over time for the ignition of a laminar propane-air mixture : experimental data from Renou and Boukhalfa [32], AVBP simulation from Enaux [11] and CEDRE simulation from the present work with two values of deposited energy.

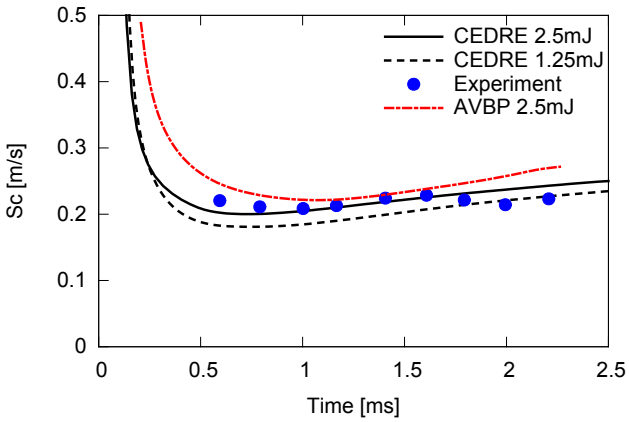

Fig. 3: Evolution of the flame propagation speed over time for the ignition of a laminar propane-air mixture : experimental data from Renou and Boukhalfa [32], AVBP simulation from Enaux [11] and CEDRE simulation from the present work with with two values of deposited energy.

At this stage, it is important to stress that using such simplified energy deposition model requires an accurate estimate of the energy amount supplied to the gas by the spark. Unfortunately, uncertainties relative to the energy deposition typically amount to 30% or more [22, 41]. The amount of energy supplied to the flow is expected to determine flame propagation in the very first instants. To verify this assumption the simulation has been run for two

values of total amount of energy supplied to the flow, 2.5 mJ and 1.25 mJ (i.e. 50%). The resulting shift is relatively minor in the laminar case, as may be seen from fig. 2. However, in a turbulent flow field and a realistic combustor geometry, the energy supplied to the gas represents a fundamental parameter to characterize the success or failure of an ignition attempt. Therefore, these uncertainties on the amount of energy supplied to the flow represent an important obstacle to the accurate prediction of ignition probabilities. While the presented methodology could be relatively accurate in the characterization of flame propagation, its use for the prediction of ignition probabilities seems questionable due to the important simplifications and uncertainties related to the characteristics of the kernel of hot gases resulting from the energy deposition process. For this reason, the present work will mainly focus on flame propagation dynamics during a successful ignition phase of the target configuration.

3 The Mercato configuration

The Mercato test rig was designed at ONERA to investigate two-phase combustion in a configuration representative of a realistic helicopter engine. This experimental facility can be operated at pressures between 0.5 bar and 1 bar and at temperatures ranging from 233 K to 473 K for the gas, allowing to reproduce high altitude conditions. The fuel is liquid kerosene and is injected at temperatures ranging from 233 K to ambient temperatures. The combustion chamber has a rectangular shape (130 mm x 130 mm) and it is equipped with Quartz windows for optical access. The air is injected into the plenum via a channel before passing through the swirler, where a rotational motion is imposed to the air. The fuel is injected at the chamber inlet via a Simplex pressure-swirl atomizer. Finally, a spark plug mounted on the wall of the combustion chamber is used for ignition. A view of the experimental setup is provided on fig. 4, while a schematic of the test rig is displayed on fig. 5. Although simplified, the Mercato configuration displays a swirler, an injection system and a spark plug which are representative of realistic aeronautical engines.

Multiple experimental campaigns were conducted for this test rig and data characterizing the purely gaseous flow and the two-phase flow in both non-reactive and reactive conditions are available [19, 34]. Furthermore, ignition probabilities and trajectories of flame kernels in the combustion chamber were measured [18, 21]. In our study, the so called reference point (see table 2) was chosen because it includes various data on both non-reactive and reactive gaseous flow and on the dispersed phase for the non-reactive case in addition to data characterizing ignition sequences.

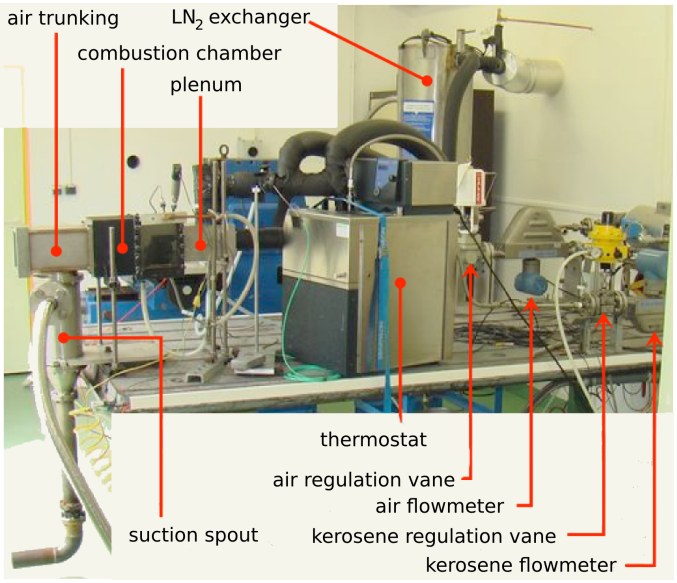

Fig. 4: View of the experimental setup for the Mercato test rig

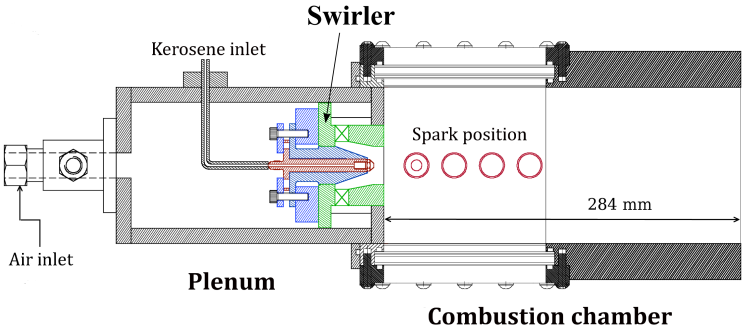

Fig. 5: Schematic of the Mercato test rig

$T_g(K)$	$\dot{m}_l(g/s)$	$\dot{m}_g(g/s)$	$P(bar)$	experimental data
293	2.25	35	1	inert and reactive : reference point [21]
463	2	15	1	inert : hot operating point [21]

Table 2: Parameters of the main operating points of the Mercato test rig. The so called reference point is simulated in the present work.

4 Validation of the non-reacting flow in the Mercato configuration

4.1 Numerical setup

The numerical simulations rely on the unsteady compressible Navier-Stokes finite-volume solver CHARME of the CEDRE platform. A Large Eddy Simu-

lation (LES) approach with the Smagorinsky sub-grid scale turbulence model [39] is employed. The main numerical parameters are summarized in table 3. An implicit second-order Runge-Kutta time integration method (RKI2) and a second-order accurate MUSCL approach in combination with a Roe scheme are used for spatial discretization. The computational domain comprises the air inlet channel, the plenum, then the combustion chamber and the suction spout, see fig. 6. In order to partially compensate for the numerical dissipation of the Roe scheme, the numerical grid was refined with respect to a reference grid used to perform LES's of the same configuration with the AVBP solver [13]. The zones of highest refinement are located inside the swirler and the first third of the combustion chamber, see fig. 6. The resulting grid is composed of approximately 3,758,000 tetrahedra, which coincides with the number of degrees of freedom since CHARME relies on a cell-centred formalism. Non reflecting boundary conditions are imposed at the in- and outlet while adiabatic laws of the wall are used to model all solid boundaries. The results of the present work were averaged over approximately 450 ms, representing approximately 8 flow through times of the combustion chamber.

Number of tetrahedra	3 758 000
Time integration	RKI2 (2^{nd} order)
Time step	$\Delta t = 10^{-6} s$
Space discretisation scheme	Roe (2^{nd} order)
Turbulence model	Smagorinsky $C_s = 0.1$
In- and outlet	Non-reflecting
Solid boundaries	Law of the wall, isothermal

Table 3: Main numerical parameters for the non-reacting simulations of the gaseous and dispersed two-phase flows

4.2 Gaseous flow

A comparison of simulation results with experimental data is shown on figs. 7 and 8 for respectively mean and root-mean square (r.m.s) axial and tangential air velocity profiles. Equally good agreement is observed for the radial velocity profiles but not shown for concision. The comparison is performed at three different planes respectively located at axial distances $z = 6$, $z = 26$ and $z = 56$ mm from the chamber inlet plane, see fig. 6. The present results are in very good agreement with experimental data as well as numerical results obtained with the AVBP solver. In particular, the opening of the jet and the magnitude of the swirling motion are very well captured. Despite some lack of convergence, velocity fluctuation levels are also in very good agreement with experiments up to the third measurement plane $z = 56$ mm. The third measurement plane is where the energy deposition will be performed for the ignition simulations

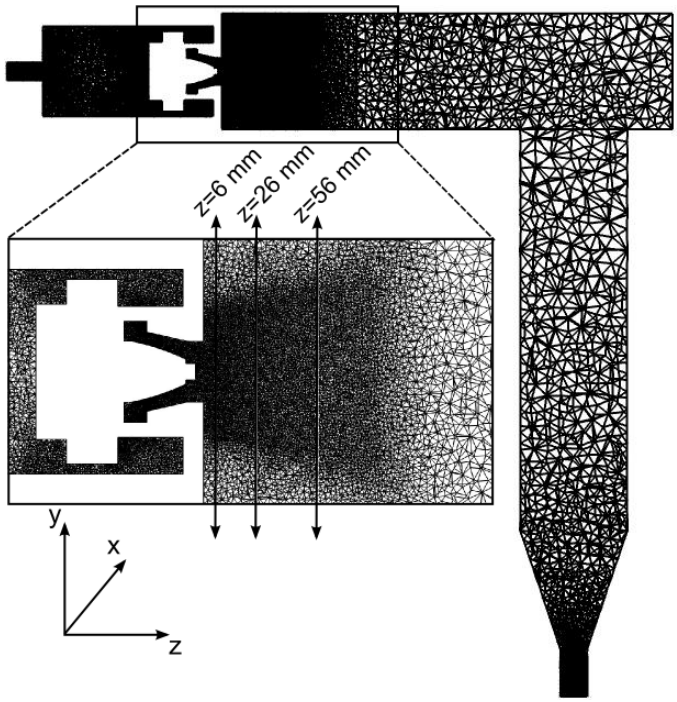

Fig. 6: Visualization of global mesh and refinements in a midplane cut along the x-axis of the computational domain and a zoom on the midplane cut through the swirler and the first third of the combustion chamber. The location of the experimental measurement planes, i.e. at z=6 mm, z=26 mm and z=56 mm is highlighted on the zoomed view.

and the present agreement indicates that fluctuations levels of the gaseous phase will be well reproduced around this region.

4.3 Two-phase flow

4.3.1 Injection procedure

The dispersed phase is described with the Lagrangian solver of the CEDRE platform named SPARTE [26]. In the Lagrangian framework, particles are treated as pointwise inclusions without explicitly resolving their surrounding flow fields. The underlying spray density function is then approximated through Dirac delta functions centred on each inclusion [43]. In the present application, the particles result from the atomization of a swirled liquid sheet. First attempts to couple the dispersed solvers of CEDRE with a diffuse interface tracking technique to model liquid atomization are currently being made [44], but they are not yet mature enough to be used for the ignition

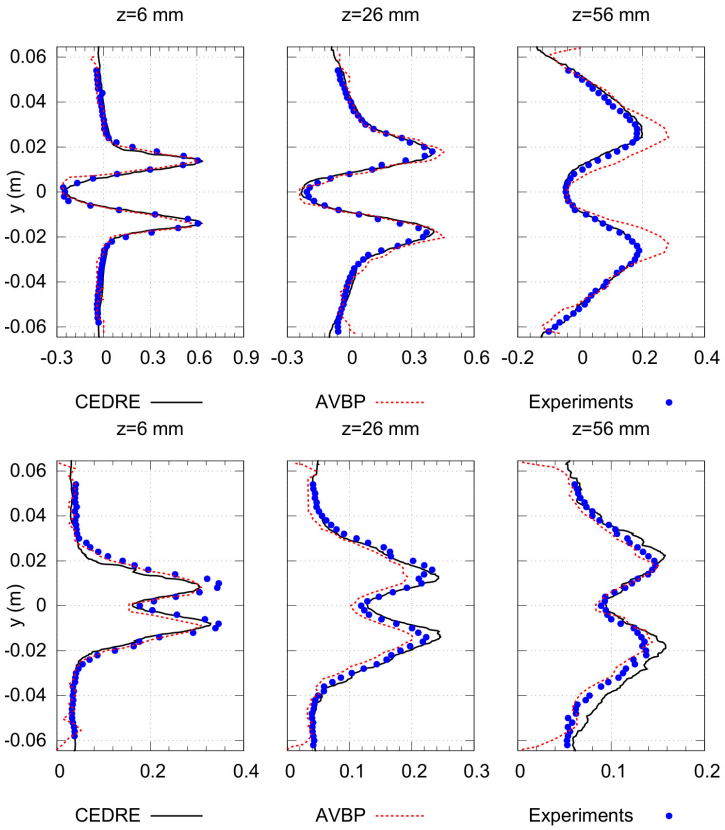

Fig. 7: Comparison of non-dimensional mean (top) and root mean square (bottom) air axial velocity profiles at several distances from the combustion chamber inlet plane. The velocities were made nondimensional by dividing them by the inlet velocity (92.45 m/s). The experimental data is represented with blue plain circles [21], simulation results of the AVBP solver [13] and CEDRE (present work) respectively appear in dashed red and plain black lines.

simulations performed in the present work. Therefore, particles are directly injected at the atomizer orifice using semi-empirical relations to specify their velocities while relying on experimental data to determine their size distribution [36]. The velocity profile used for particle injection is then made of two components, a constant axial velocity deduced from liquid mass conservation at the atomizer nozzle and an azimuthal velocity component resulting from the swirling motion imposed to the liquid within the atomizer. This swirling motion generates an air core along the axis of the atomizer such that liquid is only present between the radius of the air core R_a and the orifice radius

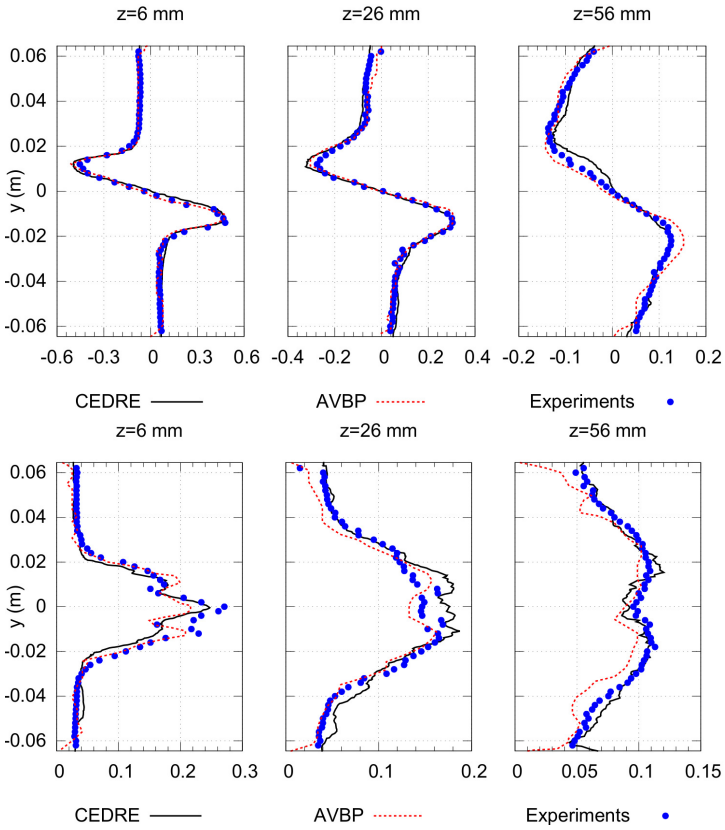

Fig. 8: Comparison of non-dimensional mean (top) and root mean square (bottom) tangential air velocity profiles at several distances from the combustion chamber inlet plane. The velocities were made nondimensional by dividing them by the inlet velocity (92.45 m/s). The experimental data is represented with blue plain circles [21], simulation results of the AVBP solver [13] and CEDRE (present work) respectively appear in dashed red and plain black lines.

R_0 [20]. The resulting velocity profile then writes:

$$u_{l,z} = \frac{\dot{m}_l}{\rho_l \pi R_0^2 (1 - X)} \tag{5}$$

$$u_{l,\phi} = \frac{\dot{m}_l}{\rho_l A_p} \frac{R_s}{r} \tag{6}$$

$$\alpha_l^0(r) = \begin{cases} 0 & \text{if } r \in [0, R_a] \\ 1 & \text{if } r \in [R_a, R_0] \end{cases} \tag{7}$$

where $R_s^0 = (R_0 + R_a)/2$ denotes the center radial position of the liquid at the atomizer orifice. The two remaining unknowns are the area ratio of the air core

Drag correlation	Schiller and Naumann [37]
Evaporation, convective effects	Ranz and Marshall [31]
Evaporation, Stefan flux	Abramzon and Sirignano [1]
Time advancement	First-order, semi-analytical [26]
Interpolation of gaseous properties	Linear
Localization algorithm	Haselbacher *et al.* [16]
Coupling between gas and particles	Two-Way
Solid boundaries	Droplet wall interaction model [35]

Table 4: Models used to describe the dispersed phase

to the nozzle X and the area of the tangential inlet ports inducing the swirling motion A_p. Both are deduced using empirical correlations of the literature [20] based on the orifice radius $R_0 = 0.5$ mm, the liquid mass flow rate $\dot{m}_l = 2.25$ $\mathrm{g\,s^{-1}}$ and the spray half angle $\theta_s^0 = 40$ °. The reader is referred to Sanjose *et al.* [36] for more details on the injection procedure. The experimental particle size distribution is approximated via a log-normal law:

$$f_n(r) = \frac{1}{\sqrt{2\pi}\sigma_{ln} r} \exp\left(-\frac{\ln(r/r_{ln})^2}{\sqrt{2}\sigma_{ln}}\right) \tag{8}$$

with r_{ln} and σ_{ln} respectively the droplet radius and the distribution variance. For the present simulations, the values $r_{ln} = 5.76 \cdot 10^{-6}$m and $\sigma_{ln} = 0.564$ were used. This simplified injection procedure was validated separately by injecting particles in a quiescent environment and verifying the imposed velocity profiles as well as the resulting size distribution (not shown).

4.3.2 Numerical setup

To evaluate the particle drag at higher particle Reynolds numbers, the correlation of Schiller-Naumann [37] is applied. A standard Spalding evaporation model [40] is used to evaluate heat and mass exchanges between the particles and the surrounding carrier phase. Convective effects are accounted for via the correlations of Ranz and Marshall [31]. In addition, the thickening of the boundary layers at the drop's surfaces due to the evaporative mass flux is accounted for using the relations of Abramzon and Sirignano [1]. Two-way coupling is enabled via the standard point force approximation [24]. The time advancement of the particles is based on a semi-analytical first order scheme. The interpolation of gaseous properties at the particle locations relies on the gradients calculated by the carrier phase solver CHARME, yielding second-order spatial accuracy. Finally, the particles are located on the computational grid using the algorithm of Haselbacher *et al.* [16]. The main numerical parameters for the dispersed phase are summarized in table 4.

4.3.3 Results

The numerical velocity and diameter fields averaged over approximately 350 ms for the dispersed phase are compared to experimental data from Linassier [21]

and simulation results obtained by Eyssartier with the AVBP solver [13] on fig. 9. It is important to note that the particle velocity data was obtained via a mass average. Also note that due to particle impingement on the windows of the chamber, a liquid film formed there and experimental data could only be acquired at a single plane located at $z = 6$mm from the chamber inlet plane. Despite a slight lack of convergence, numerical velocity profiles appear in good agreement with experimental data for the present work.

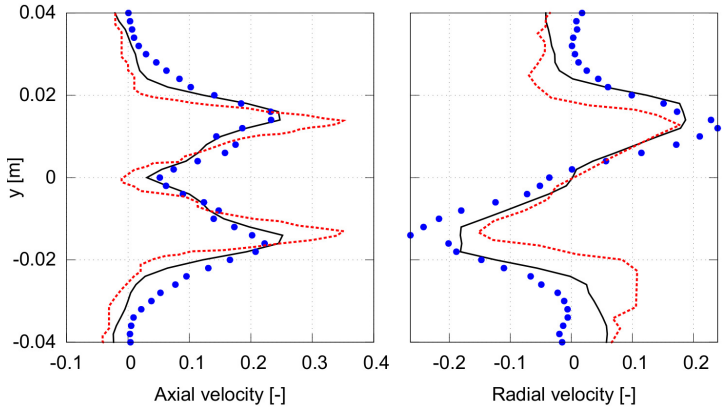

Fig. 9: Comparison of the non-dimensional mass averaged mean axial and radial velocity profiles of the dispersed phase at 6 mm from the combustion chamber inlet plane. The velocities were made nondimensional by dividing them by the inlet velocity (92.45 m/s). The experimental data is represented with blue plain circles [21], simulation results of the AVBP solver [13] and CEDRE (present work) respectively appear in dashed red and plain black lines.

As may be seen on fig. 10, numerical results are less satisfactory for the diameter distribution. Only the qualitative behaviour of an increase of the particle diameter towards the axis of the chamber is reproduced while quantitative levels are mispredicted. The overly simplified injection procedure could partly explain these differences. However, Senoner [38] obtained good agreement between numerical particle diameter profiles and experiment using the same simplified injection procedure for the hot operating point (see table 2). Also, the experimental data appear to be largely asymmetric for the arithmetic diameter profile D10 on the the left of fig. 10, which raises questions regarding the accuracy of experimental particle size measurement. Indeed it was found difficult to acquire particle data even close to the atomizer nozzle for the cold operating point as the spray is dense and particle evaporation is negligible. The particle size distribution should be further investigated but, considering the measurement uncertainties and the good prediction of the velocity, the

simulation is estimated in sufficiently good agreement with experiments to proceed with ignition simulations.

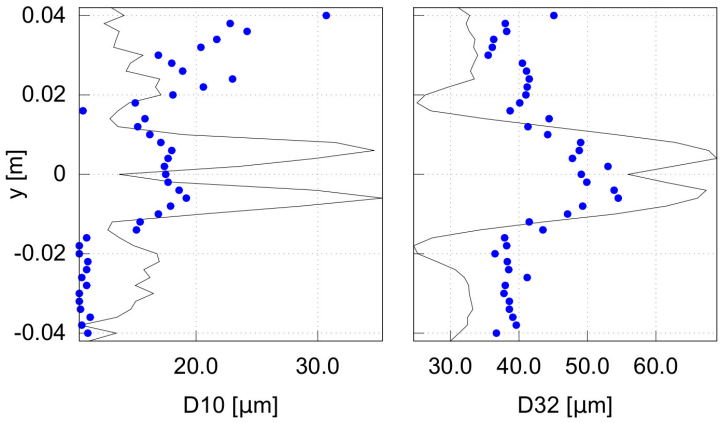

Fig. 10: Comparison of the arithmetic mean (D10) and Sauter mean (D32) diameters of the dispersed phase at 6 mm from the combustion chamber inlet plane. The experimental data is represented with blue plain circles [21], simulation results of the CEDRE platform (present work) appear in plain black lines. Numerical diameter profiles are not provided in the work of Eyssartier [13] as monodisperse Euler-Euler simulations with a particle diameter $d_p = 60\mu$m were performed.

5 Simulation of an ignition phase

After the validation of the non-reactive flow, the LES of an ignition sequence of the Mercato configuration is now simulated using the numerical parameters presented in sections 4.1 and 4.3.2 in combination with the ignition model presented in section 2.

5.1 Turbulent combustion model

In the present simulations, the chemical kinetics of kerosene rely on the BFER scheme of Franzelli *et al.* [15]. The dynamically Thickened Flame Model (TF) designed for partially premixed turbulent combustion by Colin *et al.* [8] is used. The sub-grid scale interactions between turbulence and the flame are modeled by the efficiency function proposed by Charlette *et al.* [6]. In addition, a sensor is used to detect the position of the flame front in order to limit the thickening procedure to the vicinity of the flame.

When applying the thickened flame model to dispersed two phase flows, the source terms of the carrier phase resulting from the dispersed phase need to be divided by the thickening factor [3]. This consistency correction ensures that propagation speeds of laminar spray flames remain independent of the thickening factor. This correction was validated using numerical simulations of one-dimensional saturated two-phase kerosene spray flames, see fig. 11. Note that the heat release was divided by its maximum value in each simulation. Both heat release rate and droplet diameter profiles are almost unaltered by the uniform thickening procedure compared to the reference case. On the other hand, the dynamical thickening procedure appears to slightly spread the area of significant heat release, but the integral of the latter remains almost identical. The impact of the dynamical thickening procedure on the droplet evaporation rate seems even more moderate.

5.2 Numerical setup

The numerical grid was modified with respect to the previous non-reactive simulations as significant refinement was applied to the the area of energy deposition. The characteristic local mesh size was approximately set to the laminar flame thickness to guarantee that negligible thickening was applied in the first instants of the development of the flame kernel.

In order to partly reproduce the variability of ignition, the energy deposition procedure described in section 2.1 was applied at four different instants of the two-phase flow simulations. The duration of energy deposition was deduced from experimental data and fixed to 50 µs. The amount of energy supplied to the flow was 300 mJ, which is larger than what would be expected from common estimates for the current set-up as the total electric energy supplied to the spark plug amounts to 400 mJ and energy losses are estimated at about 70%,

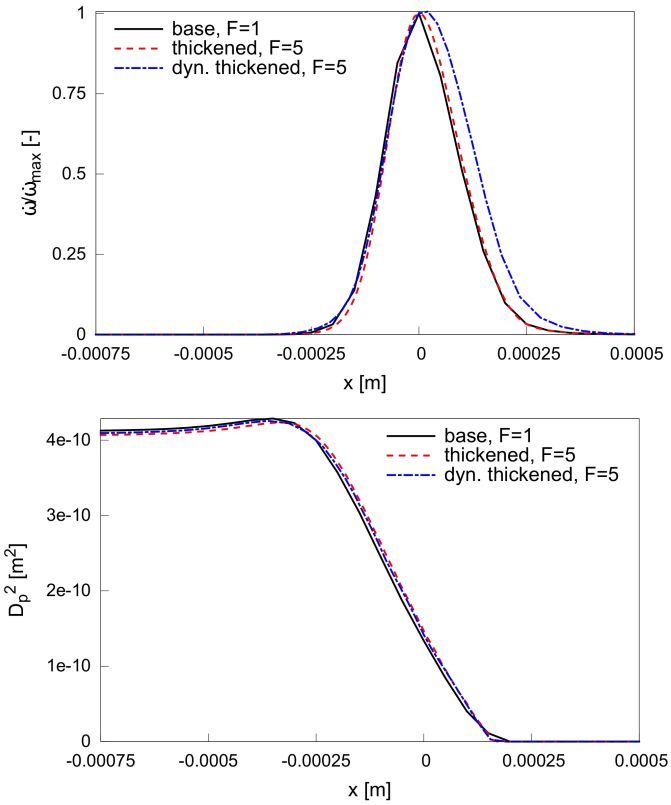

Fig. 11: Non-dimensional heat release rate and squared droplet diameter profile across a one-dimensional kerosene spray flame. Black line: reference results without thickening, i.e. $F = 1$. Red dashed line: uniform thickening applied to the entire computational domain ($F = 5$). Blue dotted line: dynamical thickening procedure based on a sensor limiting the thickening to the vicinity of the flame front ($F_{max} = 5$)

leading to an energy transfer to the flow of approximately 120 mJ. At the currently investigated spark plug location, i.e. $z = 56$ mm from the chamber inlet plane, ignition was experimentally never observed before the 9^{th} spark, which at a frequency of 6 Hz means a second and a half of fuel carburation. Therefore, the non-reactive dispersed two-phase flow simulation should have been run for the same duration in order to reproduce the experimental fuel filling of the chamber. This was however not possible for reasons of computational expense, and it was compensated by an increase in energy forcing ignition with 300 mJ after 150 ms from the start of fuel injection. At this time, the chamber seems sufficiently filled with liquid droplets to ignite. Further fueling is only expected to increase liquid volume fractions in regions where accumulation occurs, i.e. in the lateral and central recirculation zones and the chamber walls via droplet

splashing. Note that although predicted by the current droplet wall interaction model, the formation of a liquid film on the chamber walls is not explictly taken into account in the present numerical simulations. Furthermore, it was verified that the liquid volume fractions in the vicinity of the spark location fluctuate around an apparently steady mean value. The increase in the minimum ignition energy when the carburation time is reduced was observed by Neophytou *et al.* [29].

5.3 Results

Among the four ignition simulations, three led to failed ignition (extinction of the kernel while it was propagating within the chamber) and one led to a successful ignition of the Mercato test rig. In the failed ignition cases, a flame kernel was created and convected by the flow but was not strong enough to grow and eventually vanished. Snapshots of the successful ignition sequence at different instants after sparking are shown on fig. 12.

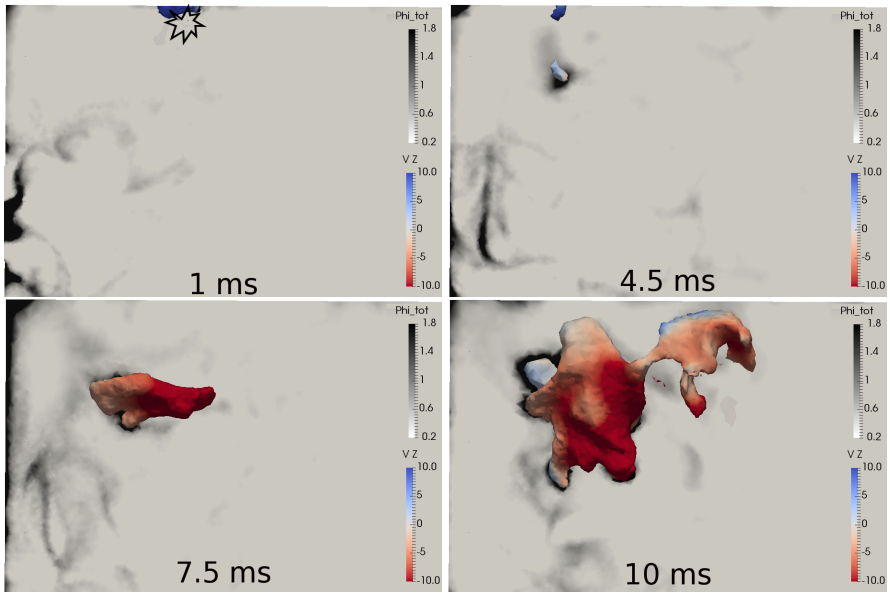

Fig. 12: Numerical snapshots of an iso-contour of temperature 1500 K colored by axial velocity on a field of total equivalence ratio at different instants after energy deposition. The spark location is schematized on the top left figure (t=1 ms).

It appears that a flame kernel forms and is convected by the flow toward a region with an equivalence ratio close to stoichiometry at about $t = 4.5$ ms after energy deposition. From this point on, a propagating flame starts and develops

in the chamber, the propagation becoming much faster after t = 7.5 ms. Note that in the failed ignition cases, the flame kernel remained in areas of low total equivalence ratio which tends to indicate that the equivalence ratio at the flame kernel location is a controlling parameter of ignition. In order to confirm this assumption with quantitative indicators, a flame consumption speed was evaluated using the following expression:

$$S_c = -\frac{1}{\rho_0 Y_{O2}^0 A_f} \int \frac{E\dot{\omega}_{O2}}{F} dV \tag{9}$$

where ρ_0 is the fresh gas density, Y_{O2}^0 the oxygen mass fraction in the fresh gas and A_f the flame area evaluated with the surface of an iso-contour $T = 1500K$. The integrated O_2 source term is the one of the Thickened Flame model, introducing the efficiency function E and the thickening factor F [8]. The temporal evolution of this flame speed is displayed on fig. 13. Besides two peak values corresponding to a vanishingly small flame area, the flame speed is contained within plausible ranges for a moderately turbulent two-phase kerosene flame, i.e. between 0.2 and 0.5 $\mathrm{m\,s^{-1}}$. The expansion of the flame kernel is visible with the increase of the area enclosing $T = 1500K$ iso-contour.

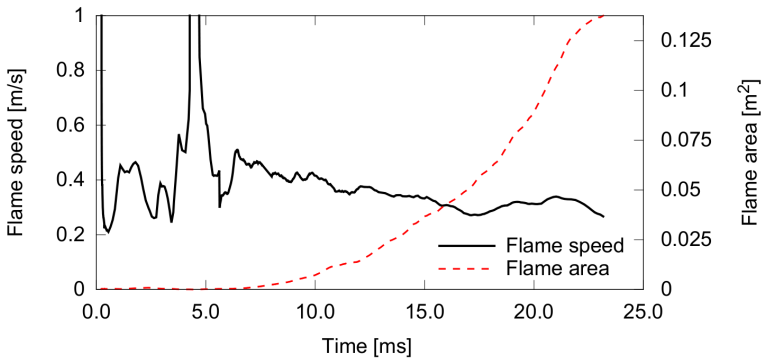

Fig. 13: Evolution of the flame consumption speed defined according to eq. 9 and the flame area identified by a temperature isosurface $T = 1500K$ over time.

A qualitative comparison with experiment based on flame visualisations at identical instants is provided in fig. 14. It is reminded that both ignition sequences occur with significantly different equivalence ratios in the chamber as ignition occurs at about 150 ms of fueling in the simulations compared to 1.5 s in the experiment. This important discrepancy clearly hinders detailed comparisons. Despite this fact, the previously identified ignition phases also seem present in the experiment as the reactive kernel is merely convected without growing until at least t = 7 ms. However, the flame propagation appears significantly faster in the simulations: it is already completed after 27 ms

whereas it lasts 39 ms in the experiment. Nevertheless, it also seems that the propagation phase is dominated by flow convection in both cases since there is approximately an order of magnitude between the observed propagation speed of the flame kernel and the turbulent flame speed. This was already observed in Boileau [4] and Philip [30] and confirms that hot gas expansion plays a key role in the full ignition of a burner. It may therefore be argued that some major features of ignition are captured in the present simulation.

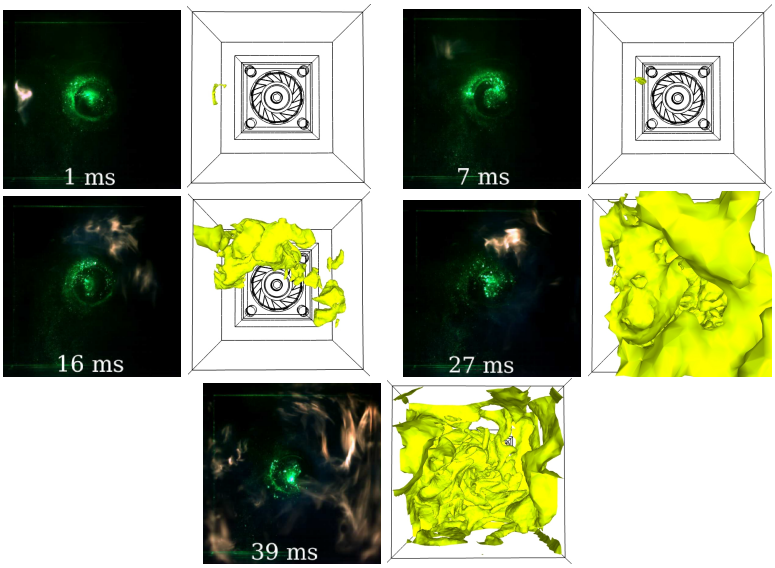

Fig. 14: Experimental tomography and simulated temperature iso-contour ($T = 1500\,\mathrm{K}$) snapshots at five different instants. The instants are indicated on the experimental snapshots and are identical for the simulation. Although the choice of the isosurface is arbitrary, it does not significantly affect the qualitative visual comparison.

6 Conclusions

The current work presented simulation results of a successful ignition sequence for the dispersed two-phase flow within the experimental test rig Mercato. Performing such ignition simulations required the implementation of simplified models describing the energy deposition process and thermophysical properties at high temperatures. These ingredients were partly validated with the simulation of a laminar freely propagating premixed flame kernel, for which present numerical results were in very good agreement with both experimental data and previous numerical results. Then, numerical simulations of the non-reacting purely gaseous and two-phase flow in the Mercato test rig were

realized for validation purposes. Results for the non-reacting gaseous flow were found in excellent agreement with experiment for both mean and root mean square velocity profiles. For the two-phase flow simulations, a simplified injection model was used and proved to yield good results for velocity profiles. However, more significant differences were observed for the size distribution profiles while global levels were in reasonable agreement. Finally, ignition simulations of the Mercato configuration were performed. Analysis of the flame behavior for a successful ignition event indicated that the flame propagation could be divided in two main phases: a convection of the flame kernel into regions of low velocity and equivalence ratios close to unity where it can grow, followed by a rapid expansion within the chamber due to convection by the flow field. These findings seem confirmed by qualitative comparisons with experiment. The flame propagation is however too fast in the simulation, which may be an artefact of the different chamber fueling between the simulation and the experiment. Overall, the results obtained in the present work show that the simulation is able to reproduce qualitatively ignition sequences. Quantitative predictions require further investigation on both experimental and numerical sides. In particular, the characteristics of the two-phase mixture at the time of ignition in the experiments would be very helpful. Work is currently ongoing on the various simplified models used here, namely the spray injection and chemical kinetic scheme.

Acknowledgements The financial support of the Direction Générale de l'Armement (DGA), the French Government Defense procurement and technology agency, is gratefully acknowledged. The authors would like to warmly thank Olivier Rouzaud, Lionel Matuszewski and Nicolas Bertier for useful discussions.

Compliance with ethical standards Loïc Hervo's PhD thesis was partially funded by the Direction Générale de l'Armement (DGA), the French Government Defense procurement and technology agency.

Conflict of Interest The authors declare that they have no conflict of interest.

References

1. Abramzon B, Sirignano WA (1989) Droplet vaporisation model for spray combustion calculations. International Journal of Heat and Mass Transfer 32(9):1605–1618, DOI https://doi.org/10.1016/0017-9310(89)90043-4
2. Aggarwal S (1998) A review of spray ignition phenomena: Present status and future research. Progress in Energy and Combustion Science 24(6):565–600, DOI https://doi.org/10.1016/S0360-1285(98)00016-1
3. Boileau M (2007) Simulation aux grandes échelles de l'allumage diphasique des foyers aéronautiques *(in French)*. Phd thesis, INP Toulouse
4. Boileau M, Staffelbach G, Cuenot B, Poinsot T, Bérat C (2008) LES of an ignition sequence in a gas turbine engine. Combustion and Flame 154(1-2):2–22, DOI https://doi.org/10.1016/j.combustflame.2008.02.006
5. Bruyat A (2012) Influence de l'évaporation de gouttes multicomposant sur la combustion et des effets diphasiques sur l'allumage d'un foyer aéronautique *(in French)*. PhD thesis, Université de Toulouse, France

6. Charlette F, Veynante D, Meneveau C (2002) A power-law wrinkling model for LES of premixed turbulent combustion. Part I - non-dynamic formulation and initial tests. Combustion and Flame 131:159–180, DOI https://doi.org/10.1016/S0010-2180(02)00400-5
7. Colin O, Truffin K (2011) A spark ignition model for large eddy simulation based on an FSD transport equation (ISSIM-LES). Proceedings of the Combustion Institute 33(2):3097–3104, DOI https://doi.org/10.1016/j.proci.2010.07.023
8. Colin O, Ducros F, Veynante D, Poinsot T (2000) A thickened flame model for large eddy simulations of turbulent premixed combustion. Physics of Fluids 12(7):1843–1863, DOI https://doi.org/10.1063/1.870436
9. Dahms R, Drake M, Fansler T, Kuo TW, Peters N (2011) Understanding ignition processes in spray-guided gasoline engines using high-speed imaging and the extended spark-ignition model SparkCIMM. Part A: Spark channel processes and the turbulent flame front propagation. Combustion and Flame 158(11):2229–2244
10. Duclos JM, Colin O (2001) Arc and kernel tracking ignition model for 3D spark ignition engine calculations. In: Fifth Int. Symp. on Diagnostics, Modelling of Combustion in Internal Combustion Engines (COMODIA), Nagoya, Japan, pp 343–350
11. Enaux B (2010) Simulation aux Grandes Echelles d'un moteur à allumage commandé - évaluations des variabilités cycliques *(in French)*. PhD thesis, Université de Toulouse , France
12. Esclapez L, Riber E, Cuenot B (2015) Ignition probability of a partially premixed burner using LES. Proceedings of the Combustion Institute 35(3):3133–3141, DOI https://doi.org/10.1016/j.proci.2014.07.040
13. Eyssartier A (2012) Study and modelisation of stationnary and transient two-phase flow combustion. PhD thesis, INP Toulouse. France
14. Eyssartier A, Cuenot B, Gicquel LY, Poinsot T (2013) Using LES to predict ignition sequences and ignition probability of turbulent two-phase flames. Combustion and Flame 160(7):1191–1207, DOI https://doi.org/10.1016/j.combustflame.2013.01.017
15. Franzelli B, Riber E, Sanjosé M, Poinsot P (2010) A two-step chemical scheme for Large-Eddy Simulation of kerosene-air flames. Combustion and Flame 157(7):1364–1373, DOI https://doi.org/10.1016/j.combustflame.2010.03.014
16. Haselbacher A, Najjar FM, Ferry JP (2007) An efficient and robust particle-localization algorithm for unstructured grids. Journal of Computational Physics 225(2):2198–2213, DOI https://doi.org/10.1016/j.jcp.2007.03.018
17. Lacaze G, Richardson E, Poinsot T (2009) Large eddy simulation of spark ignition in a turbulent methane jet. Combustion and Flame 156(10):1993–2009, DOI https://doi.org/10.1016/j.combustflame.2009.05.006
18. Lang A, Lecourt R, Giuliani F (2010) Statistical evaluation of ignition phenomena in turbojet engines. In: ASME Turbo Expo 2010: Power for Land, Sea, and Air, American Society of Mechanical Engineers, pp 985–992, DOI doi:10.1115/GT2010-23229
19. Lecourt R (2008) TIMECOP-AE WP2 D2.2.1c - Injection system two-phase flow characterisation (LDA-PDA). STREP AST5-CT-2006-030828. Tech. rep., ONERA, Fauga, France
20. Lefebvre AH (1989) Atomization and Sprays. Taylor & Francis
21. Linassier G (2012) Étude expérimentale et numérique de l'allumage des turboréacteurs en conditions de haute altitude *(in French)*. PhD thesis, Université de Toulouse, France
22. Maly R, Vogel M (1978) Initiation and propagation of flame fronts in lean CH4-air mixtures by the three modes of the ignition spark. In: 17th International Symposium on Combustion, The Combustion Institute, Pittsburgh, pp 821–831, DOI https://doi.org/10.1016/S0082-0784(79)80079-X
23. Mastorakos E (2017) Forced ignition of turbulent spray flames. Proceedings of the Combustion Institute 36(2):2367–2383, DOI https://doi.org/10.1016/j.proci.2016.08.044
24. Maxey M, Patel B (2001) Localized force representations for particles sedimenting in Stokes flow. International Journal of Multiphase Flow 27(9):1603–1626, DOI https://doi.org/10.1016/S0301-9322(01)00014-3
25. McBride BJ, Zehe MJ, Gordon S (2002) NASA Glenn coefficients for calculating thermodynamic properties of individual species. Tech. Rep. NASA/TP-2002-211556, E-13336,

NAS 1.60:211556, NASA Glenn Research Center; Cleveland, OH United States
26. Murrone A, Villedieu P (2011) Numerical modeling of dispersed two-phase flows. Aerospace Lab (2):p. 1–13
27. Neophytou A, Mastorakos E (2009) Simulations of laminar flame propagation in droplet mists. Combustion and Flame 156(8):1627–1640, DOI https://doi.org/10.1016/j.combustflame.2009.02.014
28. Neophytou A, Richardson E, Mastorakos E (2012) Spark ignition of turbulent recirculating non-premixed gas and spray flames: A model for predicting ignition probability. Combustion and Flame 159(4):1503–1522, DOI https://doi.org/10.1016/j.combustflame.2011.12.015
29. Neophytou A, Cuenot B, Duchaine P (2015) Large-eddy simulation of ignition and flame propagation in a trisector combustor. Journal of Propulsion and Power DOI https://doi.org/10.2514/1.B35792
30. Philip M, Boileau M, Vicquelin R, Riber E, Schmitt T, Cuenot B, Durox D, Candel S (2015) Large Eddy Simulations of the ignition sequence of an annular multiple-injector combustor. Proceedings of the Combustion Institute 35(3):3159 – 3166, DOI https://doi.org/10.1016/j.proci.2014.07.008
31. Ranz WE, Marshall WR (1952) Evaporation from drops. Chemical Engineering Progress 48(4):173
32. Renou B, Boukhalfa A (2001) An experimental study of freely propagating premixed flames at various Lewis numbers. Combustion science and technology 162(1):347–370, DOI 10.1080/00102200108952148
33. Richard S, Vermorel O, Veynante D (2005) Development of LES models based on the flame surface density approach for ignition and combustion in SI engines. In: ECCOMAS Thematic Conference on computational combustion, pp 1–20
34. Rosa NG (2008) Phénomènes d'allumage d'un foyer de turbomachine en conditions de haute altitude *(in French)*. PhD thesis, Institut National Polytechnique de Toulouse, ISAE
35. Rosa NG, Villedieu P, Dewitte J, Lavergne G (2006) A new droplet-wall interaction model. In: Proceedings of the 10th International Conference on Liquid Atomization and Spray System, Tokyo, Japan
36. Sanjosé M, Senoner JM, Jaegle F, Cuenot B, Moreau S, Poinsot T (2011) Fuel injection model for Euler–Euler and Euler–Lagrange large-eddy simulations of an evaporating spray inside an aeronautical combustor. International Journal of Multiphase Flow 37(5):514–529, DOI https://doi.org/10.1016/j.ijmultiphaseflow.2011.01.008
37. Schiller L, Nauman A (1935) A drag coefficient correlation. VDI Zeitung 77:318–320
38. Senoner JM (2010) Simulations aux grandes échelles de l'écoulement diphasique dans un brûleur aéronautique par une approche Euler-Lagrange *(in English)*. PhD thesis, Université de Toulouse
39. Smagorinsky J (1963) General circulation experiments with the primitive equations 1. The basic experiment. Monthly Weather Review 91:99–164, DOI 10.1175/1520-0493(1963)091⟨0099:GCEWTP⟩2.3.CO;2
40. Spalding D (1960) A standard formulation of the steady convective mass transfer problem. International Journal of Heat and Mass Transfer 1(2-3):192–207, DOI https://doi.org/10.1016/0017-9310(60)90022-3
41. Teets R, Sell J (1988) Calorimetry of ignition sparks. SAE transactions 97:371–383, DOI https://doi.org/10.4271/880204
42. Thiele M, Selle S, Riedel U, Warnatz J, Maas U (2000) Numerical simulation of spark ignition including ionization. International Symposium on Combustion 28(1):1177–1185, DOI https://doi.org/10.1016/S0082-0784(00)80328-8
43. Williams F (1958) Spray combustion and atomization. Physics of Fluids 1:541, DOI 10.1063/1.1724379
44. Zuzio D, Thuillet S, Senoner JM, Laurent C, Rouzaud O, Gajan P (2017) Multi-solver LES simulation of the atomization of a cross-flow liquid jet in a channel . In: Proceedings of the 4th INCA Colloquium, Paris-Saclay